

VORTEX FLOW CONTROL USING JUNCTURE FILLETS ON A BLUNT-NOSED, CRANKED SWEPT WING

Nikki van Luijk[1,2], Alberto van Meenen[1,3] & Roelof Vos[1,4]

[1]Delft University of Technology, Faculty of Aerospace Engineering
[2]PhD Candidate, Department of Flow Physics and Technology
[3]MSc Student, Department of Flow Physics and Technology
[4]Associate Professor, Department of Flow Physics and Technology

Abstract

This study experimentally investigates the vortex-flow-control capabilities of leading-edge juncture fillets on a blunt-nosed, cranked swept wing. Using a modular wind tunnel model, spline- and diamond-shaped fillets at the inboard-outboard wing junction are assessed through force balance measurements, oil-flow visualisation, and stereoscopic particle image velocimetry in the wake. Results show that the spline fillet generates stronger Concentrated Vortex Flows (CVFs), associated with increased lift and a delayed onset of vortex breakdown, leading to a 2.5° delay of the pitch break compared to the diamond fillet. In contrast, the diamond fillet reduces drag through delayed outboard wing flow separation, albeit with an earlier onset of vortex breakdown. These results demonstrate that small geometric modifications in the leading-edge kink of a cranked swept wing can effectively influence CVF behaviour and aerodynamic performance, revealing a trade-off between lift enhancement and predictable linear pitch behaviour.

Keywords: vortex flow, flow control, wind tunnel testing, flying wing, juncture fillets

Nomenclature

b	Semi-wing span [m]
$\bar{c}$	Mean geometric chord [m]
$c_\perp$	Local chord perpendicular to leading edge [m]
C_D	Drag coefficient [-]
C_L	Lift coefficient [-]
C_m	Pitching moment coefficient [-]
C_{m_α}	Pitching moment coefficient derivative [1/°]
M	Mach number [-]
Re_c	Reynolds number based on $\bar{c}$ [-]
u	Axial velocity [m/s]
U_∞	Freestream velocity [m/s]
x, y, z	Cartesian wind axes [m]

Greek Symbols

α	Angle of attack [°]
α_{break}	Pitch break angle of attack [°]
α_{peak}	Local peak angle of attack [°]
λ_{ci}	Swirl Strength [1/s]
ω_x	Axial vorticity [1/s]

Superscripts

$\tilde{}$	Normalized

Acronyms

CV	Coefficient of Variation
CVF	Concentrated Vortex Flow
LTT	Low Turbulence Tunnel
SPIV	Stereoscopic Particle Image Velocimetry

1. Introduction

Modern aircraft designs increasingly integrate aerodynamic efficiency with structural and volumetric functionality, as seen in blended-wing bodies and flying wings. These configurations often feature variations in leading-edge bluntness, high sweep angles, and cranked planforms that promote the formation of complex concentrated vortical flows, which strongly affect stability and control.

https://doi.org/10.71945/icas2026_0047

The FLYING V™[1] wing exemplifies this configuration class. The Flying V concept was originally conceived by German engineer Dr. Justus Benad during his internship at Airbus Hamburg [1], while researchers at Delft University of Technology conducted extensive multidisciplinary scientific research [2–7]. Its aerodynamic and flight characteristics have been investigated through wind-tunnel testing, scaled flight experiments, and flight-simulator studies, evaluating performance, flight control, and overall feasibility, and culminating in the aerodynamic design of the Flying V wing by Laar et al. [8].

This configuration features a tapered, nonslender, cranked swept wing, with a blunt inboard leading edge swept at 64° and a sharper outboard section with 39° leading-edge sweep. This geometry generates separation-induced Concentrated Vortex Flows (CVFs), driving nonlinear aerodynamic behaviour at high angles of attack, including a pitch break that limits the usable flight envelope. This instability, characterised by a persistent reversal in the pitching-moment slope from $C_{m_\alpha} < 0$ to $C_{m_\alpha} > 0$, is driven by the formation and breakdown of CVFs and outboard wing flow separation [9].

Sweep changes in cranked swept wings are known to generate CVFs that interact through merging, tearing, or re-organisation of vortex sheets, altering the surface pressure distribution [10, 11]. Since CVF formation depends on local geometry, the inboard-outboard wing junction offers an opportunity to passively influence the flow using geometric modifications called *juncture fillets*. Common geometries include linear, spline, and diamond shapes (Figure 1). A previous Flying V wing design used the baseline geometry [2], while the later design by Laar et al. [8] incorporates a spline fillet.

Early investigations into the aerodynamic effects of juncture fillets were primarily conducted on sharp-nosed double delta wings. Numerical studies by Kern [12, 13] demonstrated their potential, with the diamond fillet providing the best performance by increasing lift by 17–18% and delaying vortex breakdown. Water tunnel experiments confirmed these findings by visualising the vortex core trajectories, showing that the diamond fillet keeps the CVFs closer to the surface, thereby enhancing vortex lift [14–16]. However, the extent to which these trends persist at higher Reynolds numbers remains uncertain, as these experiments were conducted at Reynolds numbers on the order of 10^4.

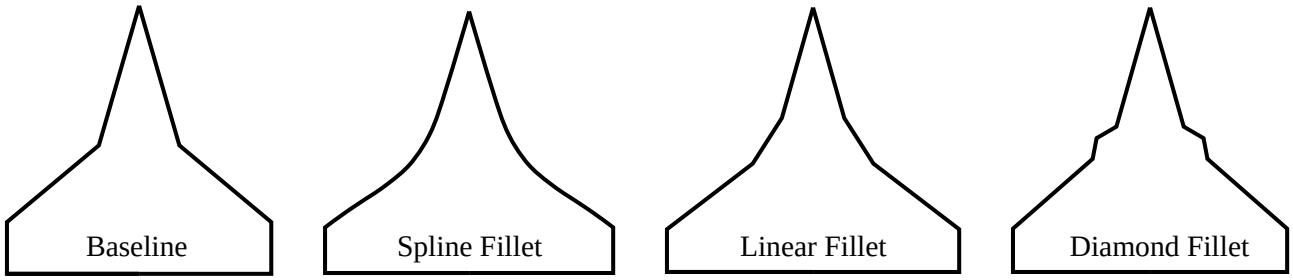


Figure 1 – Various juncture fillet shapes on a double delta wing, reproduced from ref. [15].

To investigate this, wind tunnel experiments at Mach numbers up to 0.7 and root-chord-based Reynolds numbers between 1.6–4.8×10^6 evaluated fillet performance in more detail [17]. Additional transonic tests at a Reynolds number of 2.7×10^6 extended the results to Mach 1.2 [18]. In contrast to Kern's findings [12, 13], the spline fillet produces the largest lift increase (20–39% depending on angle of attack) but also exhibits earlier asymmetric breakdown. The diamond fillet provides a lower lift increment, but shows milder nonlinear pitching-moment behaviour and delayed symmetric breakdown. At transonic speeds, however, fillet effectiveness decreases with increasing Mach number [17, 18], suggesting that these modifications may be most beneficial during take-off and landing.

While previous studies extensively examined sharp-nosed double delta wings, modern applications increasingly employ blunt-nosed configurations. Unlike sharp leading edges, CVF formation on blunt-nosed wings is governed by smooth-surface separation, which shifts the separation line downstream of the leading edge, making it sensitive to local geometry and disturbances such as roughness [19]. Consequently, it remains unclear how fillet-based flow-control methods developed for sharp delta wings translate to blunt-nosed, cranked swept wings like the Flying V configuration.

This study experimentally investigates the influence of juncture fillets on the CVF topology and aerodynamic performance of a blunt-nosed cranked swept wing, aiming to clarify how local geometric

[1] Flying V is a trademark of Fortescue. The Flying V design is owned by Fortescue, UK & NL patents pending.

modifications can enhance flow stability and extend the usable flight envelope of next-generation configurations. The experimental setup is described in Section 2., while experimental variability is presented in Section 3., followed by the results and conclusions in Sections 4. and 5.

2. Experimental Setup

This section outlines the experimental setup used to evaluate the flow-control effects of juncture fillets. The facility and model are described in Section 2.1, and the measurement techniques in Section 2.2.

2.1 Wind Tunnel Model & Facility

Measurements are conducted in the Low Turbulence Tunnel at Delft University of Technology, a closed-circuit tunnel with a turbulence intensity of 0.02% below 40 m/s. A 1.2 m-span modular model of the blunt-nosed Flying V wing designed by Laar et al. [8] is mounted upside down in the test section. The modular design allows for geometric modifications at the production breaks shown in Figure 2. The model has a mean geometric chord of 0.338 m and a reference area of 0.307 m^2. Further details on the model and wind tunnel setup are provided in Ref. [9].

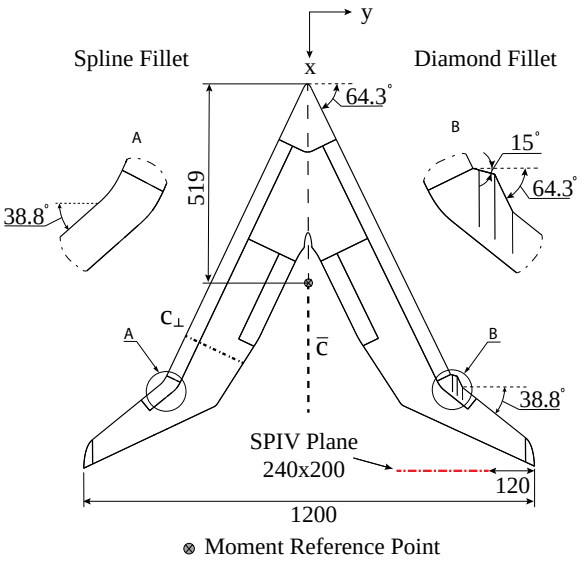


Figure 2 – Top view of the modular wind tunnel model with the spline and diamond juncture fillets (dimensions are in mm).

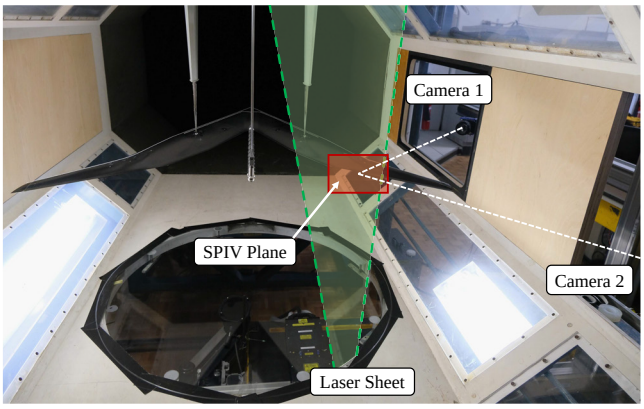


Figure 3 – SPIV setup while looking in the upstream direction. The model is mounted upside down in the test section.

Based on previous work [12–18], two promising juncture fillet geometries for delaying vortex breakdown and increasing lift are investigated: a spline and a diamond profile. The spline fillet maintains leading-edge continuity between the inboard and outboard wings, thereby suppressing the formation of a new separation line. In contrast, the diamond fillet introduces discrete discontinuities that fix the onset location of flow separation and tear the vortex sheet. The fillets, shown in Figure 2, are designed according to the guidelines of Kern [12]. Adding the diamond fillet increases the total planform area by 0.65% compared to the spline fillet configuration, which has a planform area of 0.307 m^2. It also locally increases the streamwise chord, thereby reducing the thickness-over-chord ratio.

Tests are conducted at a freestream velocity of 35 m/s, corresponding to a mean geometric chord-based Reynolds number of $Re_c = 8.0 \times 10^5$ ($\bar{c} = 0.338$ m) at Mach $M = 0.10$ for both fillets. To minimise scaling effects, boundary-layer transition is promoted using a 6 mm-wide zig-zag tape (roughness height of 0.255 mm at 70°) placed at 5% and 10% of the local chord $c_\perp$ on the suction and pressure sides, respectively. Transition downstream of the tape is verified using an acoustic probe.

2.2 Measurement Techniques

The aerodynamic effects of juncture fillets are evaluated using a six-component external balance mounted above the test section. The model is suspended upside down via a three-point suspension

system connected to the balance (Figure 3). At a test velocity of 35 m/s, the balance uncertainty is ± 0.02 N [20], corresponding to a maximum offset of $\pm 8.7 \times 10^{-5}$ in the force coefficients, which are normalised using the spline fillet's total planform area (0.307 m^2) as reference area.

No buoyancy corrections are applied, as the diverging test-section walls compensate for the streamwise pressure gradient induced by boundary-layer growth. Strut corrections are also omitted since RANS simulations and historical data [21] suggest the contributions remain below 3% for lift and pitching moment, and below 10% for drag. These offsets are therefore treated as systematic bias. This is further supported by the study's exploratory focus on relative aerodynamic differences between the fillet designs rather than on their absolute full-scale performance.

Changes in the on-surface flow topology induced by the juncture fillets are visualised using the oil-flow technique between $0^\circ < \alpha < 20^\circ$. A mixture of paraffin oil and UV-fluorescent particles is applied to the wing's suction surface, and imaged under UV illumination using a digital camera. The resulting streamline patterns can reveal separation and attachment lines, as well as CVF footprints.

The off-surface flow topology is measured using Stereoscopic Particle Image Velocimetry (SPIV) in a plane downstream of the leading-edge kink (Figure 2). An Evergreen double-pulse Nd:YAG laser with a wavelength of 532 nm illuminates the 1μm glycol seeding particles from below the test section, while two sCMOS cameras (2560×2160 pixels) with Micro-Nikkor 105 mm lenses are mounted upstream and downstream of the measurement plane at an angle of 85°, as shown in Figure 3. Calibration, acquisition, and processing are performed in LaVision's Davis 10.2 software package.

For each angle of attack, 200 image pairs are acquired at 15 Hz, and processed using an iterative multigrid approach with two passes of 96×96 pixel windows, and two passes of 48×48 pixel windows with 75% overlap, yielding a spatial resolution of 0.85 mm over a field of view of 240×200 mm. The time-averaged velocity fields are used to compute the (normalised) streamwise vorticity $\tilde{\omega}_x$ and the λ_{Ci}-criterion (swirl strength) in Tecplot 360 to quantify the effect of the juncture fillets on the CVF.

3. Data Variability & Repeatability

Beyond the uncertainties discussed in Section 2., data variability is assessed using the pitching moment coefficient, which shows the largest variation and the highest sensitivity to surface pressure. The analysis discerns within-test variation (Section 3.1) and between-test repeatability (Section 3.2).

3.1 Within-Test Variation

Within-test variability is assessed from repeated measurements within a single test campaign. As the model remained installed, reinstall effects are excluded, and variation reflects day-to-day differences such as minor alignment changes and random measurement variations.

The within-test variability for the spline fillet is based on five runs distributed over the two-week campaign. The pitching moment coefficient shows limited variation, as reflected by the Coefficient of Variation (CV) values in Table 1. The CV of C_m at $\alpha = 10^\circ$ is slightly larger than at $\alpha = 15^\circ$, as it coincides with the regime where vortex formation begins to influence the aerodynamic loads [9].

Table 1 – Within-test Coefficient of Variation (CV) of C_m and α_{break} of the spline fillet configuration.

	CV [%]		CV [%]
C_m $\alpha = 10^\circ$	1.81	$C_{m,\text{min}}$	1.97
C_m $\alpha = 15^\circ$	1.27	α_{break}	1.17
C_m $\alpha = 20^\circ$	2.12		

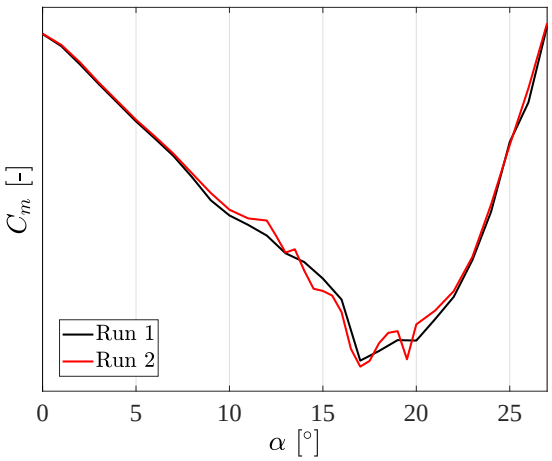


Figure 4 – Within-test variation of C_m of the diamond fillet configuration.

As the pitch break angle of attack α_{break}, defined by a persistent change in sign of the pitching moment derivative C_{m_α}, is approached, the unsteadiness in the flow increases and so does the CV at 20°. On the other hand, the CV of α_{break} is only 1.17% as it occurs between 19° and 19.5° for all runs. In general, all CV values remain below 5%, indicating good repeatability within the campaign.

The diamond fillet configuration shows a larger variation in the pitching moment coefficient, as illustrated in Figure 4. Only two runs are available, preventing the calculation of a CV. Nonetheless, the trend in the pitching moment derivative C_{m_α} differs between the two runs within the angle of attack range of $12^\circ < \alpha < 22^\circ$, indicating the sensitivity of this parameter to day-to-day experimental variations. In contrast, the pitch break location is consistently captured in both runs.

3.2 Between-Test Repeatability

Between-test repeatability is evaluated by comparing measurements of the same configuration across different wind tunnel campaigns. In contrast to within-test variation, these comparisons account for effects of model removal and reinstallation, as well as campaign-specific differences, such as trip strip application. They also capture small geometric variations, as the spline fillet was re-manufactured for this wind tunnel campaign, potentially introducing deviations due to manufacturing tolerances.

The pitching moment coefficient of the blunt-nosed cranked swept wing with the spline-shaped juncture fillet across multiple campaigns is shown in Figure 5. Individual runs are shown in grey, and the mean is shown in black. After $\alpha = 6^\circ$, two trends emerge: a continued linear decrease in C_m and a flattening of the curve with $C_{m_\alpha} = 0$. This behaviour is attributed to trip strip sensitivity, as also observed by Viet [22]. Above 12°, the trends converge, and a local peak appears between 13° and 15°, associated with outboard-wing flow separation [9]. This angle is denoted as α_{peak}. Approaching the pitch break regime, the spread between the runs increases, with α_{break} varying between 18° and 20.5° with a median of 19.5°.

The CV values in Table 2 quantify the between-test repeatability of the cranked swept wing. The CV of C_m decreases from 30.4% at 10° to approximately 13–15% at higher angles of attack, partly due to the small magnitude of C_m at low angles. The characteristic angles of attack show much smaller variability, with CV values of 5.5% for α_{peak} and 3.1% for α_{break}. Compared with the within-test CV values (Table 1), the CV of $C_{m,\min}$ and α_{break} is roughly three times larger, indicating that reinstall effects and campaign-to-campaign differences dominate the overall variability.

Although the exact values and corresponding angles of attack may vary between runs and campaigns, key aerodynamic events remain relatively consistent. This supports the use of the mean aerodynamic coefficients for comparison between the spline and diamond fillet configurations in Section 4.

Table 2 – Between-test Coefficient of Variation (CV) of C_m and characteristic angles of attack α_{peak} and α_{break} of the cranked swept wing.

	CV [%]		CV [%]
C_m $\alpha = 10^\circ$	30.4	$C_{m,\min}$	6.8
C_m $\alpha = 15^\circ$	15.1	α_{peak}	5.5
C_m $\alpha = 20^\circ$	12.7	α_{break}	3.1

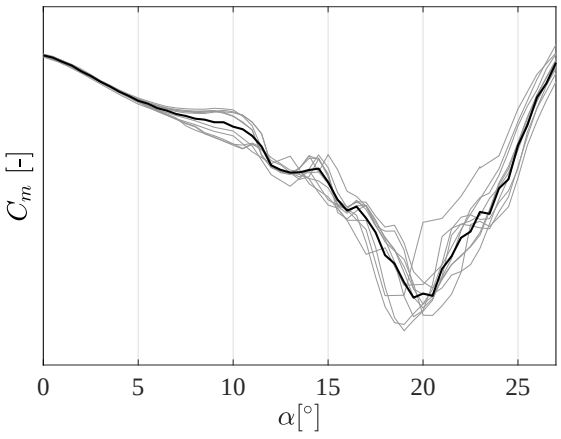


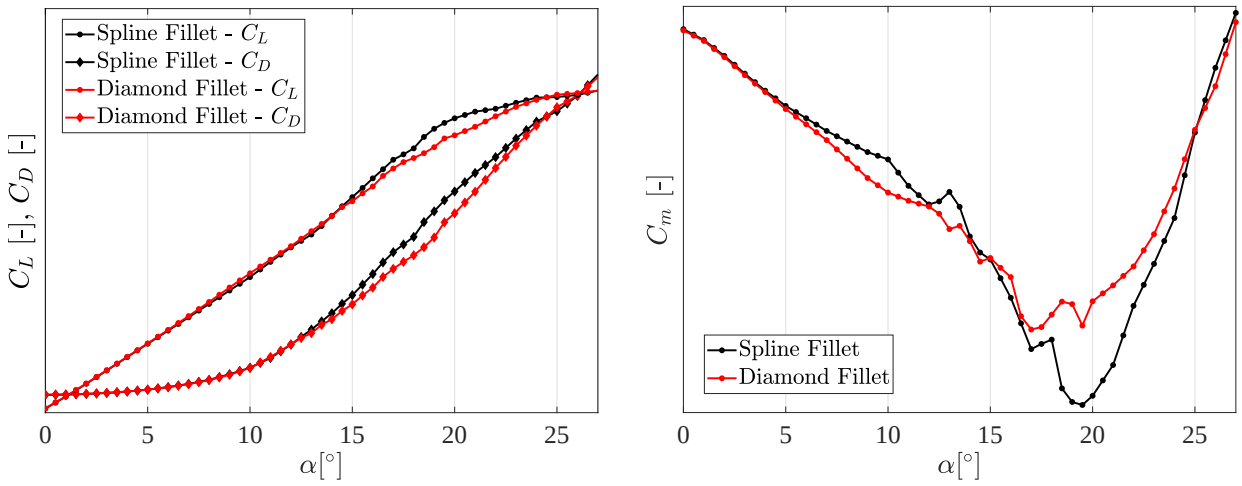
Figure 5 – Between-test repeatability of C_m of the cranked swept wing. Individual runs are shown in grey, with the mean indicated in black.

4. Results & Discussion

This section investigates the effects of spline and diamond juncture fillets on the CVFs over a blunt-nosed, cranked swept wing. Aerodynamic coefficients reveal a regime-dependent response to these geometric modifications. Both configurations exhibit similar lift-curve slopes in the linear regime, but their behaviour differs beyond $\alpha = 15^\circ$ (Figure 6a). The spline fillet produces up to 7% greater lift at $\alpha = 19^\circ$, while the diamond fillet reduces drag by up to 13% over $13^\circ < \alpha < 25^\circ$, albeit with a 1% drag penalty at $\alpha = 0^\circ$ due to its larger planform area. Consequently, the lift-to-drag ratios differ marginally, with a slight advantage of up to 3% for the diamond fillet between $12^\circ < \alpha < 21^\circ$. This lift enhancement for the spline fillet contrasts with Kern's sharp-nosed delta wing simulations [12,13] but aligns with Gonzalez et al.'s experimental findings [17,18], suggesting strong sensitivity to differences in fillet geometry and size.

The pitching-moment behaviour shows more pronounced differences, particularly in the pitch-break regime (Figure 6b). The diamond fillet produces a nearly linear C_{m_α} up to $\alpha = 16^\circ$, whereas the spline fillet displays stronger nonlinearities, including local instances of $C_{m_\alpha} > 0$. This behaviour persists until the diamond fillet's pitch break at $\alpha = 17^\circ$. The spline fillet's pitch break, which is delayed to $\alpha = 19.5^\circ$, is consistent with Gonzalez et al.'s observations of a stronger pitch-up tendency for this geometry, versus the more gradual onset for the diamond fillet [17, 18]. However, the spline fillet's increased low-angle-of-attack pitch stability observed in their study is not reproduced here.

These aerodynamic trends are linked to distinct CVF development across three flow regimes: vortical flow development ($10^\circ < \alpha < 14^\circ$, Section 4.1), vortical flow with breakdown ($15^\circ < \alpha < 16^\circ$, Section 4.2), and post-breakdown vortical flow ($17^\circ < \alpha < 20^\circ$, Section 4.3). Based on the juncture fillet's performance in each regime, their flow control capabilities are synthesised in Section 4.4.



(a) Lift and drag coefficient

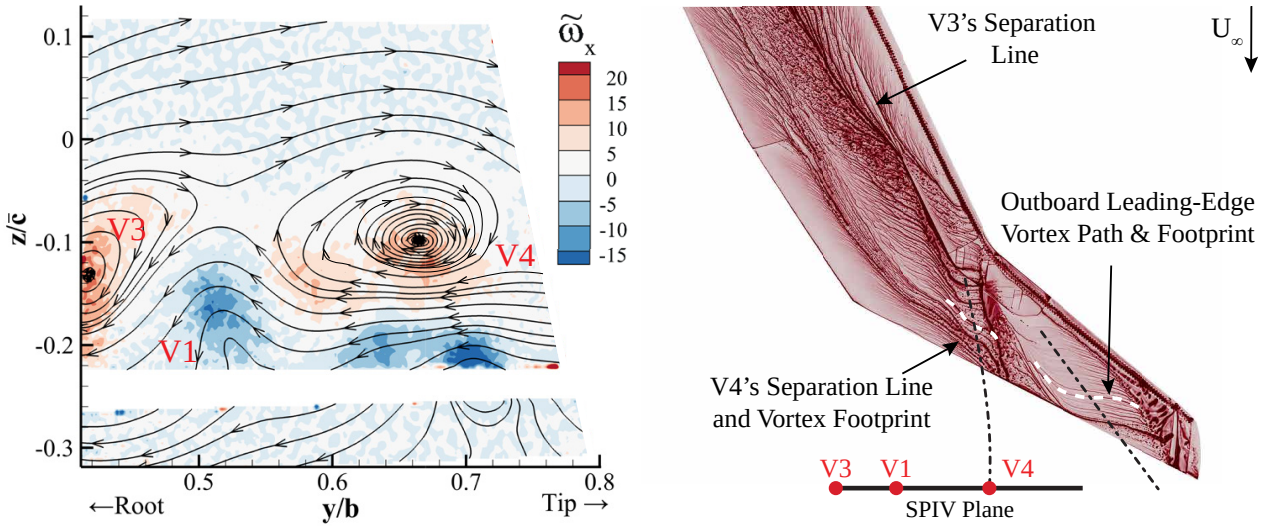
(b) Pitching moment coefficient

Figure 6 – Lift, drag, and pitching moment coefficients versus angle of attack.

4.1 Vortical Flow Development

In the CVF development regime between $10^\circ < \alpha < 14^\circ$, the spline fillet produces a coherent dual-vortex system dominated by V3 and V4 (see Ref. [9] for vortex nomenclature), as shown in Figure 7a. Following Ref. [9], which investigated the same cranked configuration, both vortices originate on the blunt-nosed inboard wing: V3 forms above the surface and lies inboard of V4, which originates near the leading edge upstream of the leading-edge kink (Figure 7b). V3 is the dominant CVF in terms of axial vorticity, reaching a maximum normalised value of $\tilde{\omega}_x = 38$ compared to $\tilde{\omega}_x = 17$ for V4.

Secondary counter-rotating structures, such as V1 forming underneath V3 on the inboard wing's trailing edge [9], do not significantly alter the primary CVF organisation as angle of attack increases. Instead, the vortex system shifts outboard without major topological changes. This migration also displaces the outboard leading-edge vortex (its path drawn in Figure 7b) toward the wing tip, reducing its influence on the primary CVF onset locations.

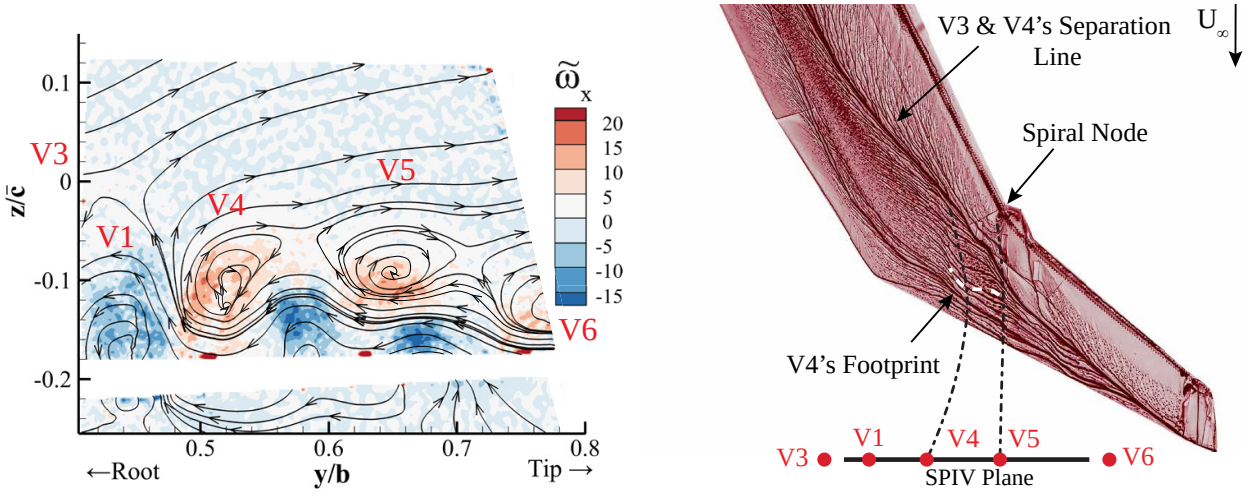


(a) Cross-flow topology with normalised vorticity

(b) Oil flow and annotated features

Figure 7 – On-surface and wake flow topology of the spline fillet configuration at $\alpha = 12.5°$.

The diamond fillet introduces additional coherent CVFs, complicating the vortex system in this flow regime (Figure 8). In addition to the primary inboard CVFs V3 (outside the SPIV field of view) and V4, extra co-rotating CVFs form: a fillet vortex (V5) from the forward edge of the diamond fillet and an outboard leading-edge vortex (V6) at the sharp fillet–wing junction, similar to those observed by Kern [12, 13]. These extra primary CVFs and their secondary counter-rotating vortices shift the separation locations and trajectories of V3 and V4 more inboard than in the spline fillet case. Consequently, CVF onset and topology are no longer governed solely by smooth-surface separation, but instead exhibit a clear direct dependence on geometry. This is evidenced by a spiral separation node [23] near the diamond fillet's forward edge in Figure 8b, indicating a fixed separation point.



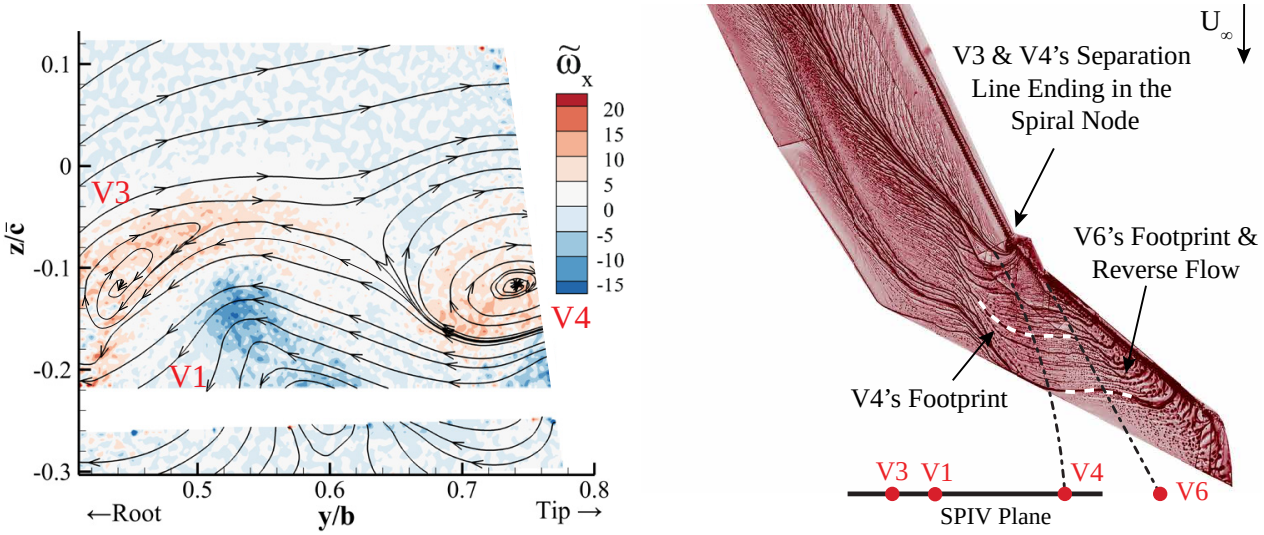
(a) Cross-flow topology with normalised vorticity

(b) Oil flow and annotated features

Figure 8 – On-surface and wake flow topology of the diamond fillet configuration at $\alpha = 10°$.

As the angle of attack rises from $\alpha = 10°$ to $12.5°$, the vortex system produced by the diamond fillet evolves toward a dual-vortex system dominated by V3 and V4, similar to the spline fillet's flow (Figure 9). However, their maximum vorticity is reduced to 43% and 74% of the spline's V3 and V4 values. The absence of V5 likely stems from the merging of the separation line of V3 and V4 into the spiral node, creating a single separation-onset location (see Figures 8b and 9b). At $\alpha = 12.5°$, the outboard wing also shows substantial reverse flow, which stays attached due to the proximity of V6 evident in the shear-stress footprint in Figure 9b.

The additional vortices (V5, V6) and V6's favourable effect on the outboard wing flow yield the diamond fillet's larger negative C_{m_α} in this regime, as shown in Figure 6b. Furthermore, the local $C_{m_\alpha} > 0$ peak at $\alpha = 13°$ for the spline fillet, which is associated with outboard wing flow separation [9], is suppressed in the diamond fillet case due to these influences.



(a) Cross-flow topology with normalised vorticity

(b) Oil flow and annotated features

Figure 9 – On-surface and wake flow topology of the diamond fillet configuration at $\alpha = 12.5°$.

4.2 Vortical Flow with Breakdown

Increasing the angle of attack to $\alpha = 15°$ reveals a similar vortex system for the spline and diamond fillet configurations, characterised by two counter-clockwise CVFs (V3 and V4) and a secondary counter-rotating vortex (V1) (Figures 10 and 11). V3 dominates in both cases, achieving a maximum streamwise vorticity of $\tilde{\omega}_x = 26$ for the spline fillet and 21 for the diamond fillet, indicating stronger rotational intensity in the former. Despite the overall similarity, the spline fillet yields more coherent CVFs with greater swirl strength. This aligns with the elevated surface suction levels generated by the spline fillet's CVFs, as reported by Gonzalez et al. [18]. In contrast, the diamond fillet shows reduced axial velocity in V4 with $u/U_\infty = 0.15$, indicating the onset of vortex breakdown. This early breakdown contrasts with previous studies, which consistently report an earlier onset of vortex breakdown for the spline fillet [12–15, 17, 18, 24].

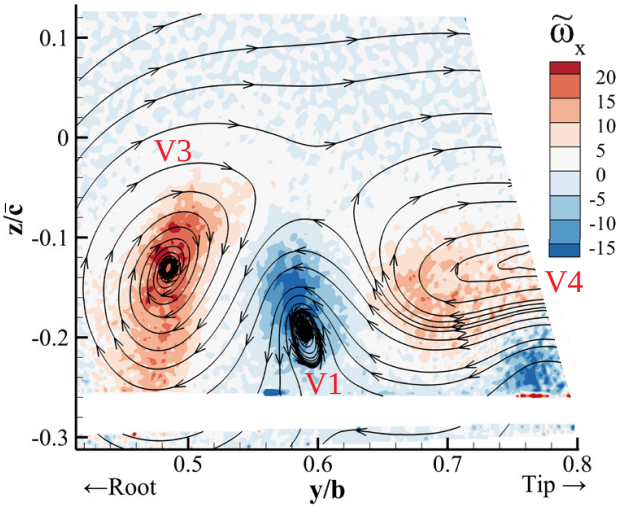


Figure 10 – Cross-flow topology of the spline fillet configuration at $\alpha = 15°$.

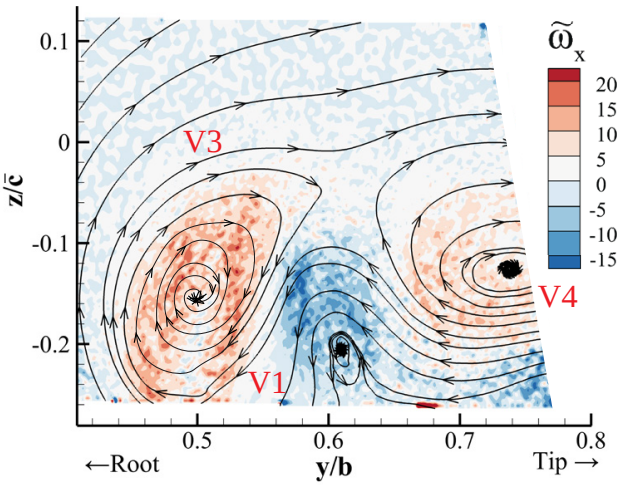
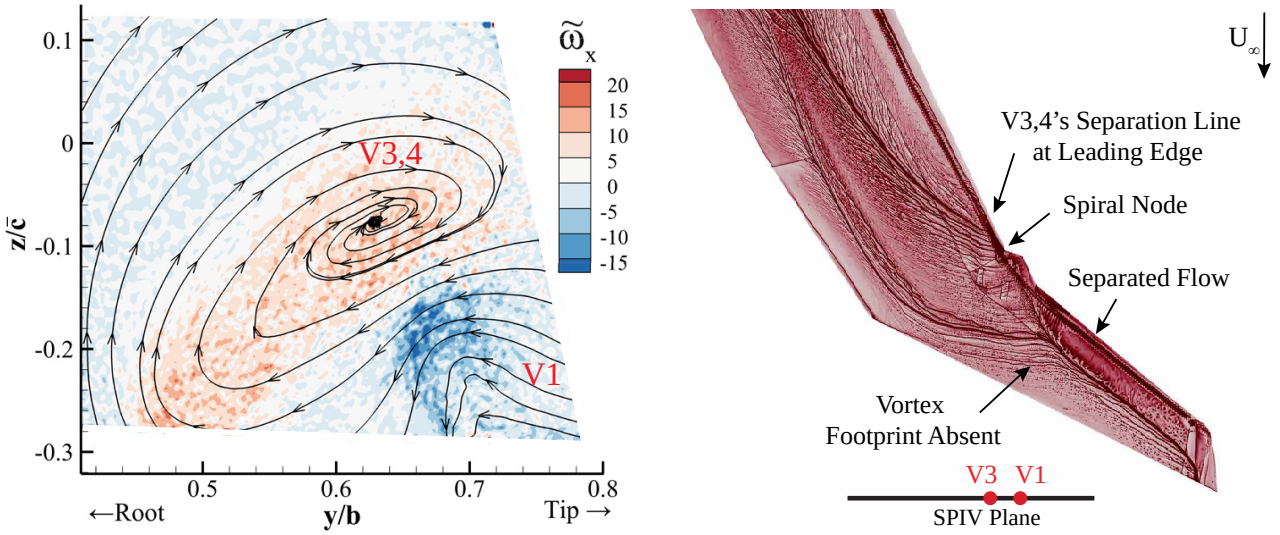


Figure 11 – Cross-flow topology of the diamond fillet configuration at $\alpha = 15°$.

The subsequent flow evolution differs significantly between the configurations. As the angle of attack increases, the spline fillet exhibits a gradual progression, with V3 intensifying and V4 slightly weakening while both shift outboard, preserving the vortex lift contribution. In contrast, the diamond fillet undergoes an abrupt change in flow topology between $15^\circ < \alpha < 16^\circ$, where the high-vorticity regions of V3 and V4 merge into a single diffuse low-vorticity structure as shown in Figure 12a. This transition is preceded by the axial stagnation in V4 at $\alpha = 15^\circ$, followed by partial momentum recovery post-breakdown ($u/U_\infty = 0.37$ at $\alpha = 16^\circ$). These observations differ from reports of V3's breakdown preceding V4 in Ref. [9]. Such discrepancies likely arise from sensitivities to the measurement techniques and the inherently unsteady dynamics of vortex breakdown.

Beyond $\alpha = 16^\circ$, the diamond fillet develops a separated flow region along the outboard leading edge (Figure 12b), accompanied by the upstream movement of the separation line of V3 and V4. Compared to lower angles of attack, where the separation line ends in the spiral node, this upstream movement indicates the earlier onset of V4. Combined with the expected upstream progression of the vortex breakdown with angle of attack [19], this reduces lift on the aft portion of the wing, shifting the centre of pressure forward and driving the pitch-up observed at $\alpha = 17^\circ$ in Figure 6b.

These topological changes are also reflected in the lift curve: the premature onset of vortex breakdown reduces the lift-curve slope of the diamond fillet in Figure 6a, while the spline fillet maintains a lift advantage due to sustained vortex lift. Despite this, the diamond fillet exhibits lower drag in this regime, indicating that the induced drag associated with the stronger, more coherent CVFs of the spline fillet exceeds the pressure losses due to vortex breakdown in the diamond fillet configuration.



(a) Cross-flow topology with normalised vorticity

(b) Oil flow and annotated features

Figure 12 – On-surface and wake flow topology of the diamond fillet configuration at $\alpha = 16^\circ$.

4.3 Post-Breakdown Vortical Flow

In the post-breakdown regime above $\alpha = 17^\circ$, the flow for both configurations converges toward a final vortex topology. The abrupt topological change first observed for the diamond fillet at $15^\circ < \alpha < 16^\circ$ occurs at a slightly higher angle of attack for the spline fillet ($16^\circ < \alpha < 17^\circ$). This results in a similar semi-coherent merged vortex (V3,4) (Figures 13 and 14). The topology observed at $\alpha = 17^\circ$ persists at higher angles of attack, highlighting the delayed but comparable breakdown progression.

With increasing angle of attack, the semi-coherent vortex expands and diffuses, as evidenced by larger regions of vorticity and swirl, alongside a diminishing axial velocity and loss of core coherence. The spline fillet experiences a stronger deceleration, decreasing from $u/U_\infty = 0.47$ at $\alpha = 17^\circ$ to 0.13 at $\alpha = 19^\circ$, before recovering to 0.34 at $\alpha = 20^\circ$. In contrast, the diamond fillet shows a milder decay, with $u/U_\infty = 0.33$ at $\alpha = 17^\circ$, which decreases to a comparable minimum of 0.15 at $\alpha = 19^\circ$, and recovers more strongly to 0.44 at $\alpha = 20^\circ$. This behaviour indicates a less severe, more gradual breakdown for the diamond fillet, consistent with observations on double delta wings [18].

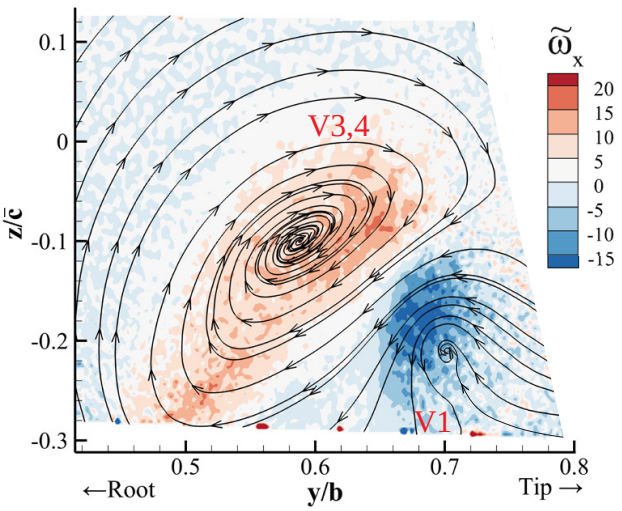


Figure 13 – Cross-flow topology of the spline fillet configuration at $\alpha = 17°$.

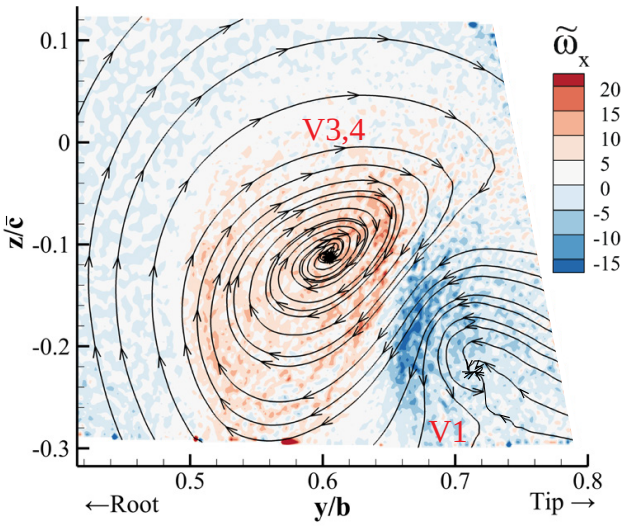


Figure 14 – Cross-flow topology of the diamond fillet configuration at $\alpha = 17°$.

The convergence toward a common post-breakdown flow topology is characterised by an upstream shift in the onset of the primary CVFs. This is evidenced by the upstream movement of the primary separation line toward the inboard leading edge for both configurations in Figures 15 and 16. Despite this convergence, the spline fillet maintains a more distinct vortex footprint, indicating greater vortex persistence near the surface. This contrasts with expectations from water-tunnel studies at low Reynolds numbers, where diamond fillets were found to promote closer surface proximity of the vortices [14, 15]. At the present wind-tunnel conditions, this reversal in trend highlights the strong Reynolds-number sensitivity of the CVFs.

The subtle differences in the post-breakdown flow characteristics are reflected in the pitching moment behaviour. A local instance of $C_{m_\alpha} > 0$ at $\alpha = 18°$ for the spline fillet suggests the development of vortex breakdown and possible oscillation of its location. The associated pitch break occurs $2.5°$ later (at $\alpha = 19.5°$) and is more abrupt than the diamond fillet's relatively gradual pitch-up. The latter aligns well with the more progressive breakdown process for the diamond fillet reported in Ref. [17, 18]. For both configurations, the strongest increase in C_{m_α} occurs beyond $\alpha = 20°$, where the aerodynamic differences diminish as the flow structures converge.

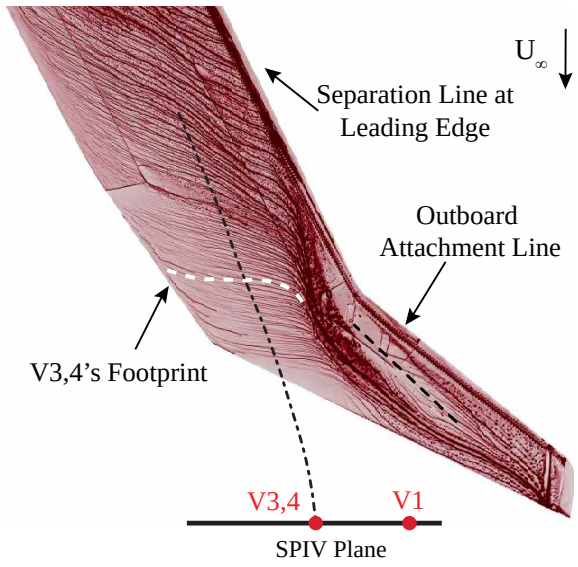


Figure 15 – On-surface flow topology of the spline fillet configuration at $\alpha = 20°$.

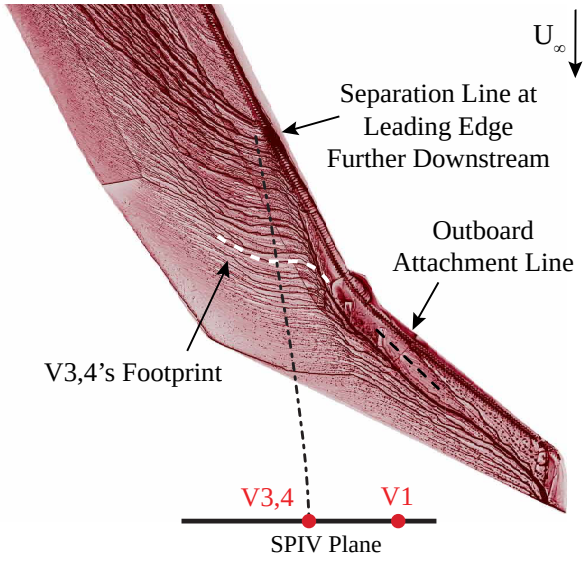


Figure 16 – On-surface flow topology of the diamond fillet configuration at $\alpha = 20°$.

4.4 Flow Control Effects

The combined aerodynamic coefficients and flow-field measurements enable a direct comparison of the flow-control mechanisms of the spline and diamond juncture fillets. Table 3 summarises their effects across the investigated angle-of-attack regimes.

In the vortical flow development regime ($10^\circ < \alpha < 14^\circ$), the spline fillet promotes a relatively simple and coherent dual-vortex system (V3 and V4) governed by smooth-surface separation on the blunt inboard wing. The resulting CVF topology remains stable with increasing angle of attack, but is sensitive to local separation behaviour. This produces moderate nonlinearities in the pitching moment coefficient. In contrast, the diamond fillet introduces additional coherent CVFs (V5 and V6) originating at the fixed geometric discontinuities. These act as controlled separation points, reducing reliance on smooth-surface separation and enabling controlled vortex onset. As a result, the diamond fillet produces a more predictable flow organisation and a more linear pitching moment slope.

In the moderate angle-of-attack regime ($15^\circ < \alpha < 16^\circ$), the flow of the two configurations begins to differ. The spline fillet maintains coherent and gradually evolving CVFs, producing substantial vortex lift. On the other hand, the diamond fillet exhibits an earlier onset of vortex breakdown, which reduces the vortex lift and introduces nonlinearities in the pitching moment. At the same time, attachment of reverse flow over the outboard wing is promoted, mitigating separation-induced drag.

In the post-breakdown regime ($17^\circ < \alpha < 20^\circ$), both configurations converge toward a semi-coherent merged vortex topology. The spline fillet undergoes a delayed but more abrupt breakdown, resulting in an aggressive pitch-up. Nonetheless, CVFs ahead of the breakdown location remain close to the wing's surface, ensuring sustained vortex lift. Although the diamond fillet displays an earlier onset of vortex breakdown, the subsequent breakdown progression is more gradual. This reduces lift and increases C_{m_α} more gradually post-pitch-up. Consequently, the diamond fillet offers improved longitudinal stability at the expense of maximum lift performance.

Overall, the spline fillet acts as a lift-enhancement device by promoting strong, coherent CVFs and delaying vortex breakdown, while the diamond fillet acts as a geometric flow-control device that regulates local separation and improves stability ahead of the pitch-up. This results in a clear trade-off between maximising aerodynamic performance in terms of lift and achieving improved stability and predictability in complex vortex-dominated flows.

Table 3 – Comparison of vortex flow behaviour and aerodynamic effects for spline and diamond fillets.

Regime	Spline Fillet	Diamond Fillet
$10^\circ < \alpha < 14^\circ$	• Dual CVF system driven by smooth-surface separation • Stable topology with increasing α • Sensitive to local separation $\rightarrow$ moderate C_m nonlinearity	• Geometry-driven CVFs (fixed separation) • Reduced sensitivity to surface behaviour • More linear C_m response
$15^\circ < \alpha < 16^\circ$	• Strong, coherent CVFs • Gradual vortex evolution with α • Sustained vortex lift	• Earlier vortex breakdown • Reduced vortex lift • Reverse-flow attachment lowers drag
$17^\circ < \alpha < 20^\circ$	• Delayed but abrupt breakdown • Sustained vortex lift ahead of breakdown • Strong pitch-up in C_m	• Gradual breakdown progression • Reduced lift • More gradual C_{m_α} increase post pitch-up

5. Conclusion and Future Outlook

This study investigates the effects of juncture fillets on the vortical flow over a blunt-nosed, cranked swept wing, with a focus on aerodynamic performance and vortex control. The results demonstrate that relatively small geometric modifications to the leading-edge kink between the inner and outer wing parts can significantly alter the development of vortices at moderate to high angles of attack, their breakdown behaviour, and the resulting aerodynamic characteristics.

In this study, two fillet types are experimentally characterised: a spline fillet and a diamond fillet. The spline fillet enhances lift at angles of attack above 15°, yielding up to 7% more lift than the diamond fillet due to increased vortex persistence, and delaying the pitch break by approximately 2.5°. In contrast, the diamond fillet has lower drag between 13° and 25°, likely associated with reduced induced drag and a delayed onset of outboard-wing flow separation. However, the diamond fillet does promote an earlier onset of vortex breakdown around 16°, leading to a positive pitching moment gradient from 17° onward as breakdown progresses upstream.

These results reveal a trade-off between performance and stability. The spline fillet produces extra lift and delays the pitch-up due to vortex persistence. In contrast, the diamond fillet promotes favourable local flow behaviour, resulting in a more linear pitching-moment behaviour at lower angles of attack and reduced drag.

Future work should focus on optimising the fillet geometry depending on the desired aerodynamic effect. Moreover, modifications to the inboard wing geometry, where the primary vortices originate, could offer further potential for flow control, particularly to improve the pitching moment behaviour across the full angle-of-attack range. Combining such modifications with a diamond fillet may enable configurations that promote stable, predictable pitch behaviour, which is relevant to the development of blunt-nosed, cranked swept configurations such as blended-wing bodies and flying-wing designs.

6. Contact Author Email Address

Mail to: N.L.M.vanLuijk@tudelft.nl

7. Copyright Statement

The authors confirm that they, and/or their company or organization, hold copyright on all of the original material included in this paper. The authors also confirm that they have obtained permission, from the copyright holder of any third party material included in this paper, to publish it as part of their paper. The authors confirm that they give permission, or have obtained permission from the copyright holder of this paper, for the publication and distribution of this paper as part of the ICAS proceedings or as individual off-prints from the proceedings.

References

[1] Benad J. The Flying V – a new aircraft configuration for commercial passenger transport. In *Proceedings of the Deutscher Luft- und Raumfahrtkongress (DLRK)*, pages 1–8, 2015. doi:10.25967/370094.

[2] Palermo M. and Vos R. Experimental aerodynamic analysis of a 4.6%-scale Flying V subsonic transport. In *AIAA SciTech 2020 Forum*, Orlando, FL, USA, January 2020. American Institute of Aeronautics and Astronautics. doi:10.2514/6.2020-2228.

[3] Ruiz Garcia A., Brown M. T. H., Atherstone D. M., van Arnhem N., and Vos R. Aerodynamic model identification of the Flying V from sub-scale flight test data. In *AIAA SciTech 2022 Forum*, Virtual Event, 2022. American Institute of Aeronautics and Astronautics. doi:10.2514/6.2022-0713.

[4] van Overeem S., Wang X., and van Kampen E. Handling quality improvements for the Flying-V aircraft using incremental nonlinear dynamic inversion. In *AIAA SciTech 2023 Forum*, National Harbor, MD, USA, January 2023. American Institute of Aeronautics and Astronautics. doi:10.2514/6.2023-0105.

[5] Desiderio M., Schuurman M., Alderliesten R., and Castro S. G. P. Crashworthiness of the Flying-V aircraft concept with vertical drop test simulations. EngrXiv preprint, 2024. doi:10.31224/3034.

[6] Kumar A., Asaro S., and Vos R. Aerodynamic analysis of the Flying V subsonic transport to enable engine integration. In *AIAA SciTech 2025 Forum*, Orlando, FL, USA, January 2025. American Institute of Aeronautics and Astronautics. doi:10.2514/6.2025-0666.

[7] Asaro S., Atmaca D., van Kampen E.-J., and Vos R. Control surface allocation based on offline handling quality simulations for a flying wing aircraft. *CEAS Aeronautical Journal*, 2025. Springer. doi:10.1007/s13272-025-00906-2.

[8] Laar Y., Atherstone D., Benad J., and Vos R. Aerodynamic design of a Flying V aircraft in transonic conditions. In *AIAA SciTech 2024 Forum*, Orlando, FL, USA, January 2024. American Institute of Aeronautics and Astronautics. doi:10.2514/6.2024-2669.

[9] van Luijk N. and Vos R. Experimental investigation of vortex flow over a Flying V subsonic transport. In *AIAA SciTech 2025 Forum*, Orlando, FL, USA, January 2025. American Institute of Aeronautics and Astronautics. doi:10.2514/6.2025-0258.

[10] Hoeijmakers H., Vaatstra W., and Verhaagen N. On the vortex flow over delta and double-delta wings. In *3rd Joint Thermophysics, Fluids, Plasma and Heat Transfer Conference*, St. Louis, MO, USA, June 1982. American Institute of Aeronautics and Astronautics. doi:10.2514/6.1982-949.

[11] Verhaagen N. Investigation of the vortex flow over a 76/60-deg double-delta wing at 20 deg incidence. In *9th Applied Aerodynamics Conference*, Baltimore, MD, USA, September 1991. American Institute of Aeronautics and Astronautics. doi:10.2514/6.1991-3208.

[12] Kern S. B. A numerical investigation of vortex flow control through small geometry modifications at the strake–wing junction of a cropped double-delta wing. In *30th Aerospace Sciences Meeting and Exhibit*, Reno, NV, USA, January 1992. American Institute of Aeronautics and Astronautics. doi:10.2514/6.1992-411.

[13] Kern S. B. Vortex flow control using fillets on a double-delta wing. *Journal of Aircraft*, 30(6):818–825, 1993. doi:10.2514/3.46422.

[14] Hebbar S. K., Platzer M. F., and Khozam A. Investigation into the effects of juncture fillets on the vortical flow over a cropped double-delta wing. In *32nd Aerospace Sciences Meeting and Exhibit*, Reno, NV, USA, January 1994. American Institute of Aeronautics and Astronautics. doi:10.2514/6.1994-626.

[15] Hebbar S. K., Platzer M. F., and Khozam A. Experimental investigation of vortex flow control using juncture fillets on a cropped double-delta wing. In *33rd Aerospace Sciences Meeting and Exhibit*, Reno, NV, USA, January 1995. American Institute of Aeronautics and Astronautics. doi:10.2514/6.1995-649.

[16] Hebbar S. K., Platzer M. F., and Chang W.-H. Control of high-incidence vortical flow on double-delta wings undergoing sideslip. *Journal of Aircraft*, 34(4):506–513, 1997. doi:10.2514/2.2220.

[17] Gonzalez H. A., McLachlan B. G., Erickson G. E., and Bell J. H. Effects of various fillet shapes on a 76/40 double-delta wing from Mach 0.18 to 0.7. In *RTO AVT Symposium on Advanced Flow Management: Part A – Vortex Flows and High Angle of Attack for Military Vehicles*, Loen, Norway, May 2001. NATO Research and Technology Organization. RTO-MP-069(I), published 2003.

[18] Gonzalez H. A. and Erickson G. E. Pressure-sensitive paint investigation of double-delta wing vortex flow manipulation. In *43rd Aerospace Sciences Meeting and Exhibit*, Reno, NV, USA, January 2005. American Institute of Aeronautics and Astronautics. doi:10.2514/6.2005-1059.

[19] Luckring J. M. and Rizzi A. Prediction of concentrated vortex aerodynamics: current CFD capability survey. *Progress in Aerospace Sciences*, 147:100998, 2024. doi:10.1016/j.paerosci.2024.100998.

[20] Bernardi S. and Molenwijk L. Korte kalibratie van de balansen van de lage turbulentie windtunnel. Technical report, Delft University of Technology, Delft, The Netherlands, 2008.

[21] van Arnhem N. *Unconventional propeller–airframe integration for transport aircraft configurations*. PhD thesis, Delft University of Technology, Delft, The Netherlands, 2022.

[22] Viet R. Analysis of the flight characteristics of a highly swept cranked flying wing by means of an experimental test. Master's thesis, Delft University of Technology, Delft, The Netherlands, 2019.

[23] Peake D. J. and Tobak M. Three-dimensional separation and reattachment. NASA Technical Memorandum NASA-TM-84221, NASA Ames Research Center, Moffett Field, CA, USA, March 1982.

[24] Hebbar S. K., Platzer M. F., and Chang W.-H. Juncture fillets for vortex flow control on double-delta wings undergoing sideslip. In *34th Aerospace Sciences Meeting and Exhibit*, Reno, NV, USA, January 1996. American Institute of Aeronautics and Astronautics. doi:10.2514/6.1996-663.